mining

MDPI

Article

Spatiotemporal Analysis of Total Suspended Solids in Water Bodies and Mapping Mining Areas in Suriname and French Guiana

Breno Mello Pereira [1] and Felipe de Lucia Lobo [2,*]

[1] Engineering Center (CEng), Universidade Federal de Pelotas (UFPel), Pelotas 96010-610, RS, Brazil; brenomello178@gmail.com
[2] Center for Technological Development (CDTec), Universidade Federal de Pelotas (UFPel), Pelotas 96010-610, RS, Brazil
* Correspondence: felipe.lobo@ufpel.edu.br; Tel.: +55-(53)-99998-7181

Abstract: Artisanal and small-scale gold mining (ASGM) has made several environmental impacts, resulting in the significant siltation of water bodies due to the deposition of sediments on riverbanks. Based on this perspective, this study aims to investigate the water bodies and regions most impacted by mining activities, especially in relation to the increase in the Total Suspended Solids (TSS) caused by ASGM, focusing on the territories of Suriname and French Guiana, over the period from 2017 to 2023, through the creation of an algorithm in Google Earth Engine. This research also aims to map and describe active mining in this region using the Classification and Regression Tree (CART) method, which achieved an overall accuracy of 82% and a kappa index of 0.77. The results reveal that from 2017 to 2024, there was an increase of 148.09 km^2 in mining, with an average increase in TSS of up to 167 mg/L in water bodies most affected by mining activities. Finally, the continued importance of using remote sensing technologies, such as GEE, together with innovative methodological approaches, to monitor and manage natural resources in a sustainable manner is highlighted.

Keywords: mining; total suspended solids; environmental monitoring; remote sensing; Google Earth Engine; image classification

Citation: Pereira, B.M.; Lobo, F.d.L. Spatiotemporal Analysis of Total Suspended Solids in Water Bodies and Mapping Mining Areas in Suriname and French Guiana. *Mining* **2024**, *4*, 510–529. https://doi.org/10.3390/mining4030029

Academic Editors: Chengyu Xie, Jian Zhou, Danial Jahed Armaghani, Qingfa Chen and Wei Pan

Received: 1 May 2024
Revised: 4 July 2024
Accepted: 11 July 2024
Published: 16 July 2024

1. Introduction

The global gold mining industry generally focuses on large companies, but in many parts of the world, especially in developing countries, mineral extraction is predominantly driven by artisanal and small-scale gold mining (ASGM), forming a diverse and complex sector [1,2].

ASGM is a widespread practice in developing countries in the Americas, Asia, and Africa [3–5]. In the Amazon, this activity began in the 1950s in areas known as mining and currently involves hundreds of thousands of people due to the increase in gold prices in recent years [6].

Despite its economic importance, ASGM (Figure 1) has caused several environmental impacts, being one of the main drivers of deforestation globally [7], causing significant geomorphic changes to the terrain [8], including mercury contamination, the sedimentation of waterways, and environmental degradation [4,9]. This practice results in the significant siltation of water bodies due to the deposition of sediments on riverbanks, where the exploitation of alluvial deposits is common [2]. This affects water quality, increasing the Total Suspended Solids (TSS) and reducing the penetration of sunlight necessary for the production of organic matter by aquatic organisms [10], in addition to impacting fish [11] and benthic communities [12].

River sedimentation is a globally recognized problem in gold mining regions such as Indonesia, Ghana, French Guiana, and Peru, where most operations take place on

riverbanks or directly in riverbeds [11]. This process significantly contributes to the increase in suspended solids in the water, damaging the quality and health of aquatic ecosystems. In the Brazilian Amazon, sediment resulting from mining can reach one or two tons per gram of gold produced [4], further intensifying this problem.

Figure 1. Illustration of artisanal or semi-industrial gold mining activities in French Guiana [13]. From top left to bottom right: (**a**) mechanical removal of surface soil horizons, (**b**) stripping off of gold-bearing material with water jets to recover gold particles and nuggets, (**c**) digging of a derivation canal, (**d**) settling basin, and water turbidity in Combat Creek (**e**) before and (**f**) during artisanal small-scale gold mining activities.

Furthermore, the accumulation of sediment in riverbeds can alter river channel morphology, affecting the availability of suitable habitats for various aquatic species, such as obstructing fish spawning areas and destroying important habitats such as sandbars and rocky bottoms, essential for the life cycle of many species.

Artisanal and small-scale mining (ASM) causes harmful effects due to the extraction and processing of minerals with hazardous chemicals; the poor management of mining waste; and insufficient restoration, remediation, and rehabilitation activities [8]. These factors not only harm the natural environment, but also put human health at risk.

The 2023 State of the Industry Survey [8] reveals several environmental impacts of ASM, many of which are associated with the negative health effects on populations involved in ASM and local communities. Soil erosion, deforestation, the contamination of streams and wetlands, soil pollution, and dust emission are the environmental impacts most frequently mentioned in the Mine Site Questionnaire [8].

In recent years, malaria epidemics have been reported in French Guiana and Suriname in regions where these mining activities occur, aggravated by the presence of a highly concentrated vulnerable population without access to healthcare [8]. Additionally, this malaria was then spread when the highly mobile artisanal and small-scale miners returned home [14].

Another negative point of artisanal and small-scale gold mining (ASGM) in the Amazon is associated with socioenvironmental conflicts, such as human rights violations and the misappropriation of lands from indigenous communities that trigger conflicts and tensions.

In this context, this research aims to fill a significant gap in the analysis of the environmental impacts of gold mining in often-neglected areas of the Amazon, specifically in the territories of Suriname and French Guiana. While gold mining in the Brazilian Amazon has been widely studied and documented, mining activities in these adjacent regions, although equally relevant in terms of environmental and socioeconomic impact, often do not receive the same attention from the scientific community and policymakers.

Given that many of these settlements operate informally within remote protected areas and indigenous lands in the Amazon, the use of satellite imagery to delineate historic and active mining areas as well as spectral assessments of water quality via remote sensing becomes the only viable tool for a more accurate understanding of changes in river water quality related to gold mining practices in the region. This set of information, which includes changes in land use and water quality associated with artisanal and small-scale gold mining (ASGM), is of great interest to land managers as it helps in assessing the social and environmental implications of the activities of gold mining. At the same time, these data are essential to inform the development of public policies aimed at recovering degraded areas and promoting the sustainable use of water and mineral resources in the region [6,9,11].

Based on this perspective, this study's main objective is to investigate the water bodies and regions most impacted by mining activities, especially in relation to the increase in the Total Suspended Solids (TSS) caused by artisanal and small-scale gold mining (ASGM) in the Amazon, focusing on the territories of Suriname and French Guiana, over the period from 2017 to 2023, through the creation of an algorithm in Google Earth Engine. This research also aims to map and describe active mining in this region, drawing a parallel with their proximity to the most affected water bodies. In doing so, we seek to provide insights into patterns of mining activity and associated environmental effects, contributing to a more comprehensive understanding of the impacts of gold mining in these neglected areas of the Amazon.

2. Materials and Methods

2.1. Research Area

The study area (Figure 2) refers to northeast Suriname and northwest French Guiana, covering the northern portion of the Amazon. The extension coordinates are as follows: top left, −55.7909, 6.0316 (longitude, latitude); bottom right, −52.6653, 3.0696 (longitude, latitude).

In this polygon, the mapping of mines will occur throughout its extension, while the analysis of the TSS will focus on the main water bodies in the region, including Lake Brokopondo, Lake Sinnamary, the Maroni River, and the Suriname River. These bodies of water play fundamental roles in local ecosystems and are essential for the lives of the communities that inhabit this area of the Amazon.

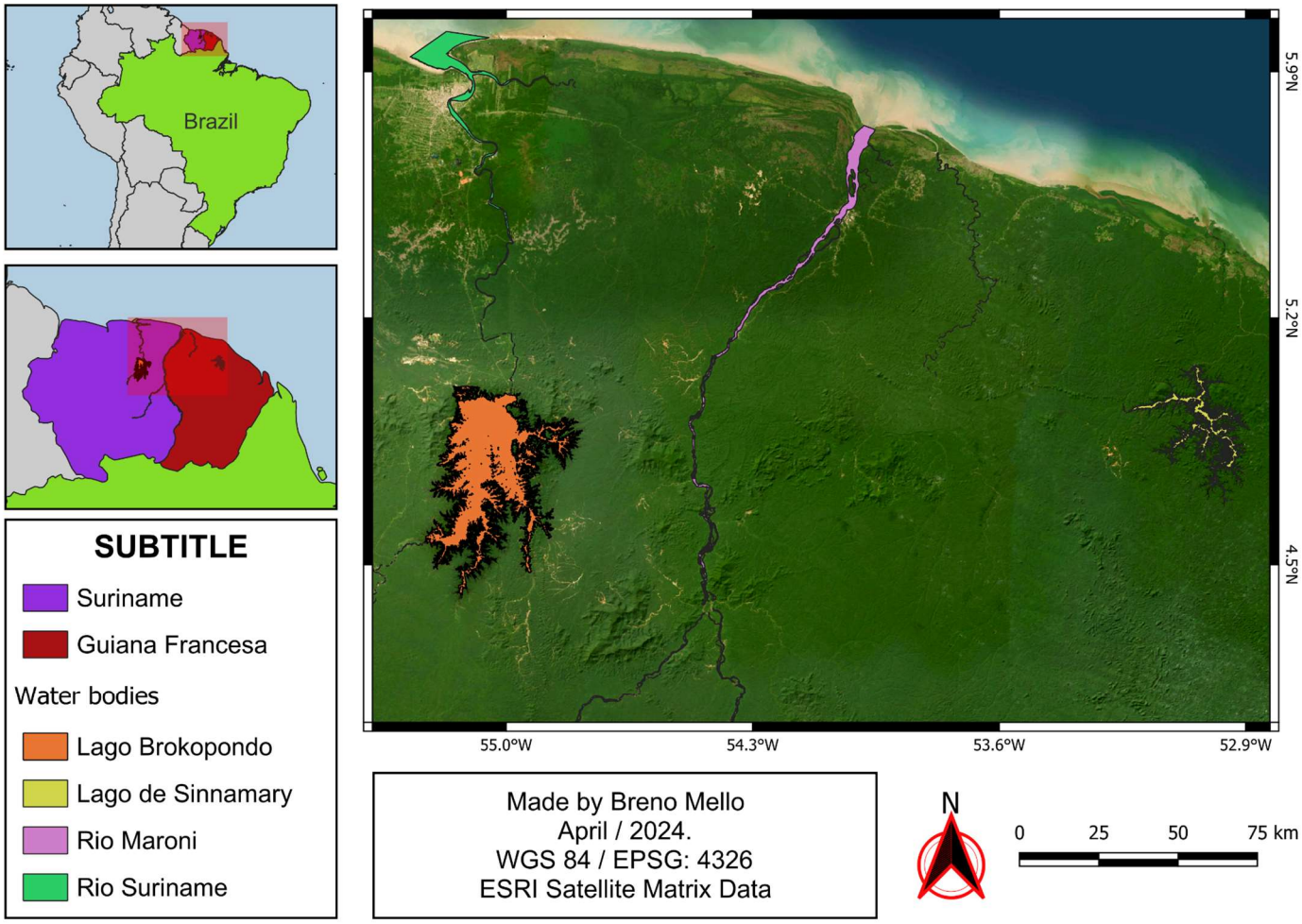

Figure 2. Study area.

2.2. Overall Methodological Workflow

Below, we present the methodological flowchart (Figure 3) of this study, in which we detail the steps divided between pre-processing, processing, and the final results. In pre-processing, we process the Sentinel image collection from 2017 to 2023 and perform filtering to remove clouds. In processing, we apply the TSS to the water bodies of interest and map the mining areas. The final result includes the products obtained for spatiotemporal analysis, visualization, and download.

The first stage of this study involved creating the algorithm in Google Earth Engine (GEE). GEE is a cloud-based geospatial image processing and analysis platform that offers a broad set of data and tools for spatial and temporal analysis. Its ability to process large volumes of data quickly and efficiently makes it a powerful tool for environmental monitoring studies and spatiotemporal analysis.

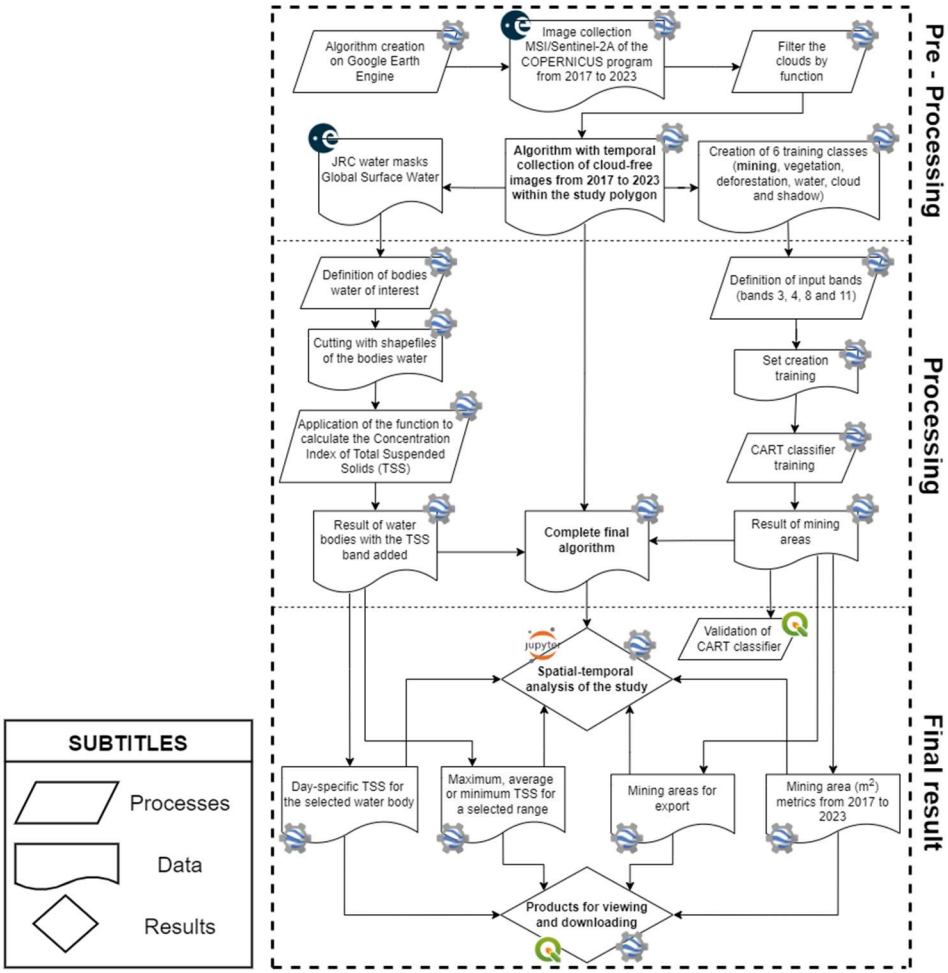

Figure 3. Overall methodology.

2.2.1. Imagery Time-Series for Monitoring Water Quality and Mining Areas

To monitor water quality and mining areas over time, an approach based on a time series of satellite images was used. Specifically, images from the Sentinel-2A satellite (Table 1), belonging to the Coperni2us program, were used due to its high spatial resolution and revisit frequency suitable for environmental studies.

Table 1. Sentinel-2A bands table [15].

Band	Name	Spectral Range (nm)	Spatial Resolution (m)
Band 1	Coastal aerosol	443	60
Band 2	Blue	490	10
Band 3	Green	560	10
Band 4	Red	665	10
Band 5	Red Edge 1	705	20
Band 6	Red Edge 2	740	20
Band 7	Red Edge 3	783	20
Band 8	NIR (Near Infrared)	842	10
Band 8A	Narrow NIR	865	20
Band 9	Water vapor	945	60
Band 10	SWIR—CIRRUS	1375	60
Band 11	SWIR 1	1610	20
Band 12	SWIR 2	2190	20

This collection contains previously atmospherically corrected and harmonized images, ensuring the consistency and quality of the data throughout the analyzed period.

To select suitable images, the following code was used:

```
var collection = ee.ImageCollection("COPERNICUS/S2_SR_HARMONIZED")
    .filterDate('2017-01-01', '2023-12-31')
    .filterBounds(geometry3)
    .filter(ee.Filter.lt('CLOUDY_PIXEL_PERCENTAGE', 10));
```

This code allows you to filter the Sentinel-2 image collection for the period of interest (from January 2017 to December 2023) and restrict the study area through the spatial delimitation defined by the variable "geometry3". Furthermore, the "CLOUDY_PIXEL_PERCENTAGE" filter was used to select only images with less than 10% cloud cover, ensuring the quality of the data used in the analysis.

Despite limiting the analysis to images with a cloud coverage of 10% or less, the challenge of correctly classifying the TSS values was still identified, as some of them actually corresponded to covered areas by clouds. Considering this issue, a more sophisticated cloud filter was implemented, which now removes pixels affected by clouds during the final classification step.

Below is the implemented code:

```
var s2Clouds = ee.ImageCollection('COPERNICUS/S2_CLOUD_PROBABILITY')
.filterBounds(region1)
.filterDate(fromDateSentinel, toDateSentinel);
var s2_orig = ee.ImageCollection('COPERNICUS/S2_SR_HARMONIZED')
.filterBounds(region1)
.filterDate(fromDateSentinel, toDateSentinel);
var MAX_CLOUD_PROBABILITY = 10;
function maskClouds(img) {
  var clouds = ee.Image(img.get('cloud_mask')).select('probability');
  var isNotCloud = clouds.lt(MAX_CLOUD_PROBABILITY);
  return img.updateMask(isNotCloud); }
function maskEdges(s2_img) {
  return s2_img.updateMask(
    s2_img.select('B8A').mask().updateMask(s2_img.select('B9').mask()));}
  s2_orig = s2_orig.map(maskEdges);
var s2SrWithCloudMask = ee.Join.saveFirst('cloud_mask').apply({
primary: s2_orig,
secondary: s2Clouds,
condition: ee.Filter.equals({leftField: 'system:index', rightField: 'system:index'})});
var s2CloudMasked = ee.ImageCollection(s2SrWithCloudMask).map(maskClouds);
```

The "maskClouds" and "maskEdges" functions are used to mask clouds in images (Figure 4). The first function masks the pixels affected by clouds, while the second function masks the edges of the images.

After applying the cloud and edge masks, the two collections are combined using the "ee.Join.saveFirst" function. Finally, a new collection of images where the clouds have been masked is created, using the "map" function to apply the "maskClouds" function to all images in the combined collection, from 2017 to 2023.

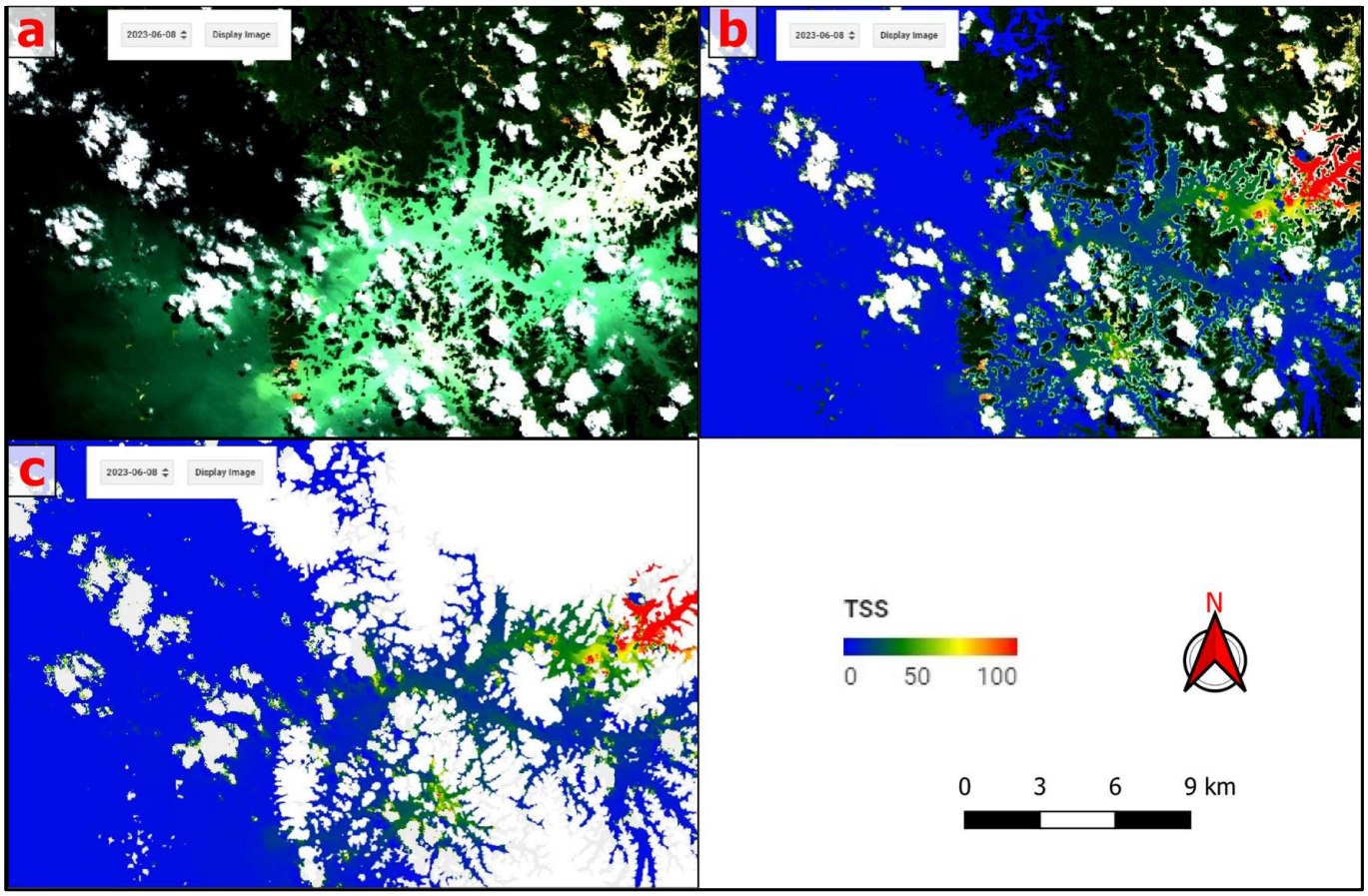

Figure 4. Practical demonstration of the filter. From top left to bottom right: (**a**) Sentinel-2A image from 8 June 2023 over Lake Brokopondo, with the presence of clouds, (**b**) TSS classification over the original image, (**c**) classification after removing the clouds.

Mapping of Mining Areas

In the collection of images processed from 2017 to 2023, in order to map the mining areas, the first step was to define the land cover classes for training; with prior knowledge of the study area and the mining context present in the region, six classes were defined (Table 2): water, vegetation, deforestation, cloud, cloud shadow, and mining. Due to the spectral difference of these 6 targets of interest being distinct, the classification process is subsequently facilitated.

Table 2. Class training table.

Training Class	Number of Samples
Mining	100
Water	40
Vegetation	30
Cloud	30
Shadow	30
Deforestation	30
Total	260

Figure 5 below illustrates the process of training classes on satellite images to identify mining areas.

After training, the Classification and Regression Tree (CART) method was applied, which is a non-parametric classifier that does not require any a priori statistical assumptions regarding the distribution of the data.

CART is a classification method that operates at the pixel level and uses the pixel intensities of training samples (polygons) to build a decision tree that assigns a class to each pixel in the image (20 m). Bands 3 (560 nm), 4 (665 nm), 8 (842 nm), and 11 (1610 nm) were used, selected based on their spectral properties and ability to provide relevant information for classifying areas of interest.

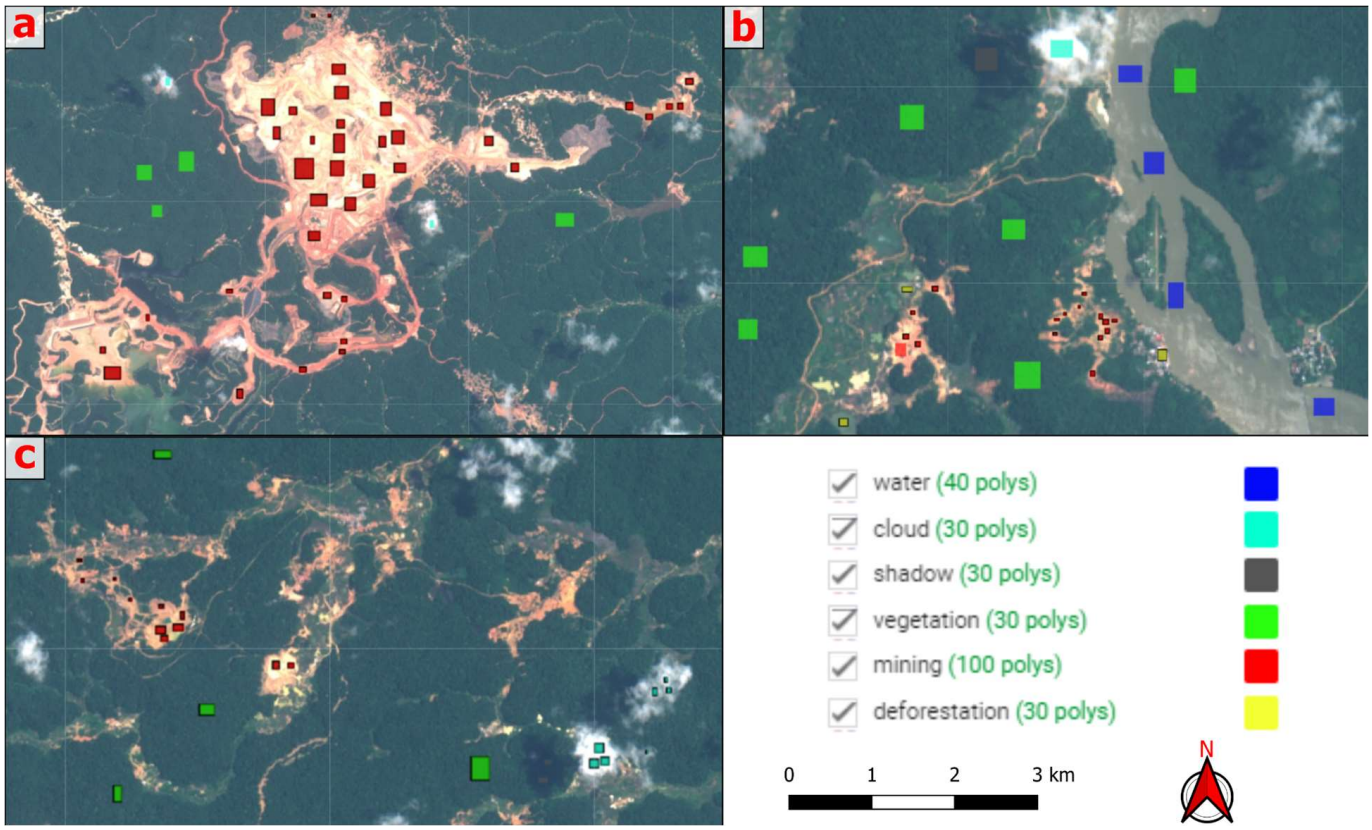

Figure 5. Demonstration of some points used in training. From top left to bottom right: (**a**) training of an extensive mining area, (**b**) training of a small mining area next to a water body, (**c**) classification of another mining area south of Lake Brokopondo.

In Google Earth Engine, the CART algorithm (ee.Classifier.smileCart) is configured with two parameters: MaxNodes, which determines the maximum number of leaf nodes in each decision tree, and MinLeafPopulation, which establishes the minimum number of points required in a set training tool to create a node. These parameters have been set to default values: no limit on the maximum number of nodes and one on the minimum number of points for creating nodes.

The CART classification (Figure 6) proved to be effective in differentiating the six classes of interest, including the precise detection of mining areas, which subsequently underwent a validation process, which is further discussed in the results.

The resulting layer was exported to the Tiff file type in Google Drive for further analysis and discussion.

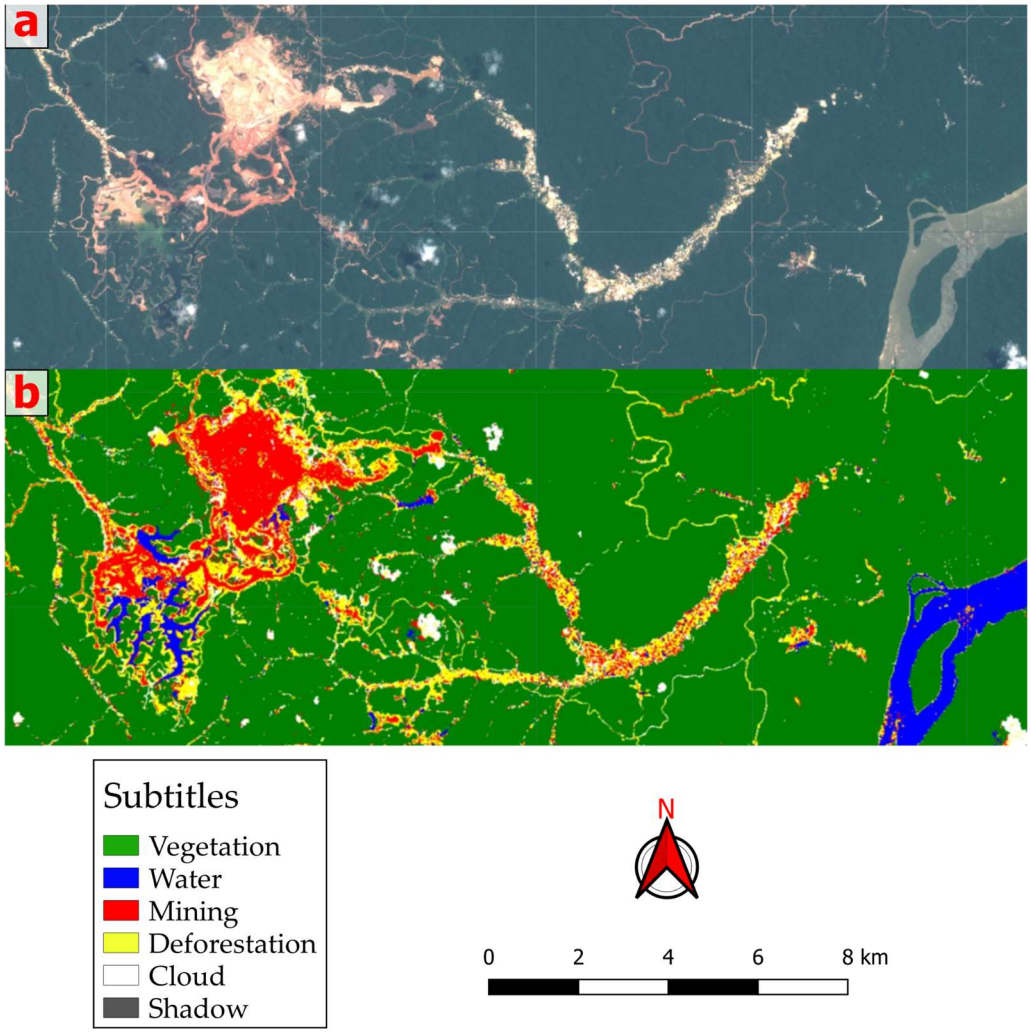

Figure 6. CART classification. From top to bottom: (**a**) Sentinel-2A image (9 January 2023) of a mining area northeast of Lake Brokopondo, (**b**) result of CART classification with the 6 classes.

Monitoring Water Quality

The use of satellite sensors combined with remote sensing techniques has been used to estimate TSS in coastal and inland waters [16,17].

This approach to estimating suspended solids in water generally follows two distinct approaches: empirical, which is based on the direct correlation between measured TSS and satellite data [18]; and analytical methods, which depend on the measured optical properties of water [19,20]. This research demonstrates that the green and red bands have a significant relationship with TSS up to approximately 100 mg/L. The use of the red band to estimate TSS in waters through empirical regressions is well documented in the literature. Previous studies, such as those by Harrington et al. [17] and Mertes et al. [21], for MSS data demonstrated this approach comprehensively.

For this study, a robust empirical model was implemented between in situ TSS and the red band of the TM sensor on the Landsat 5 satellite, established from two field campaigns in the Amazon to measure radiometric quantities and concentrations of TSS, described in detail in Lobo et al. [18].

In order to recover the TSS concentration from the surface reflectance, a non-linear regression was established between TSS and ÿsurf(red) derived from reference images, in which it was observed that the best empirical correlation between TSS and ÿsurf (ÿ) was given by a power function (R^2 = 0.94, RMSE = 1.33%) using the red band [18].

Even though the curve was constructed based on data from the ÿsurf(red) satellite up to 22%, it is believed that this function can be extrapolated to values up to 35%. This equates to approximately 300 mg/L TSS [18]. It is important to note the strong correlation between TSS and in situ ÿsurf(red).

Briefly, a model was developed that correlates SST measurements in the field with the red band of the Landsat 5 and Sentinel-2A satellites. This model uses red band reflectance to calculate SST concentrations in water. The data demonstrated a strong correlation between measured and predicted values, confirming the effectiveness of the model for accurate SST estimates from satellite imagery.

The non-linear regression obtained for the Landsat 5 TM sensor, described previously, was adapted for Sentinel-2A. So, the script in Google Earth Engine looked like this:

```
var TSS = function(image) {
    var TSSn = image.expression(
            '((RED/2.64)**(1/0.45)) + 2.27', {
              'RED': image.select('B4').multiply(0.01)})
            var TSSname = TSSn.rename(['TSSn']);
          return TSSname;}
```

This function calculates the TSS from the spectral bands of the Sentinel-2A image. First, the red band of the image is selected, represented by the variable "RED". Then, the pixel values from that band are converted to reflectance by multiplying them by 0.01, as the original values are in digital counting units (DN). The formula for calculating TSS is then applied to the converted red band. After calculation, the result is renamed to "TSSn" to represent the Total Suspended Solids (TSS). Finally, the function returns the resulting TSS image (Figure 7), where each pixel represents the TSS estimate based on the red band of the Sentinel-2A image.

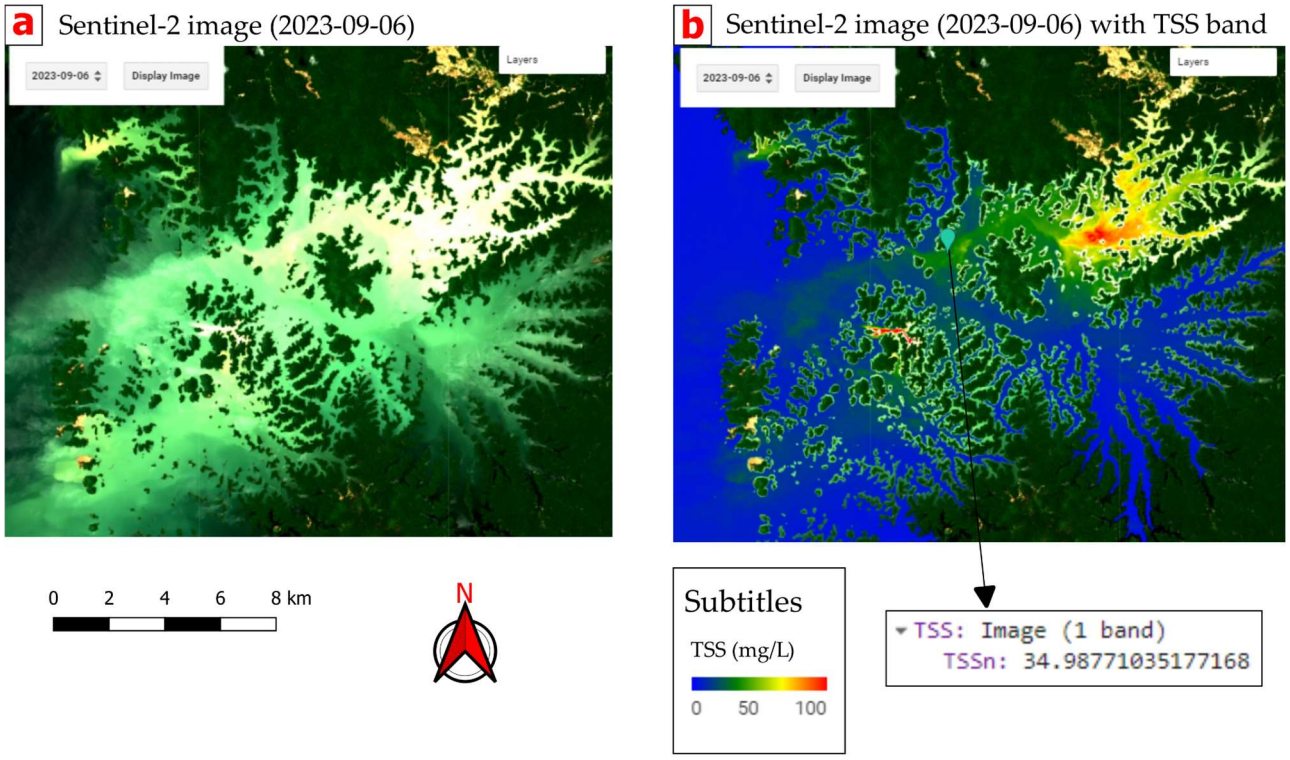

Figure 7. Illustrative image of the TSS classification in the algorithm in Google Earth Engine. From left to right: (**a**) Sentinel-2 image from 6 September 2023 and (**b**) Sentinel-2 image from the same day with the TSS classification band (mg/L) added.

From this new band, the following processes were carried out with the analysis of the TSS in all water bodies in the extension of the study area based on the collection of previously treated images from Sentinel 2, from 2017 to 2023.

3. Results

3.1. Validation of Gold Mining Areas

In the process of validating mining areas, the accuracy of the CART classification used here was evaluated. The objective was to evaluate the reliability of the classification results obtained from the analysis of satellite images. This assessment was crucial to ensuring the credibility of the identified mining sites for subsequent analysis and decision-making processes.

To conduct validation, a total of 50 mining points (Figure 8) were established across the study area. Each validation point was visually inspected using high-resolution imagery from Google Earth Pro, which utilizes high-resolution image mosaics. Specifically, images from Maxar Technologies, 2024 Airbus, and CNES/Airbus were used.

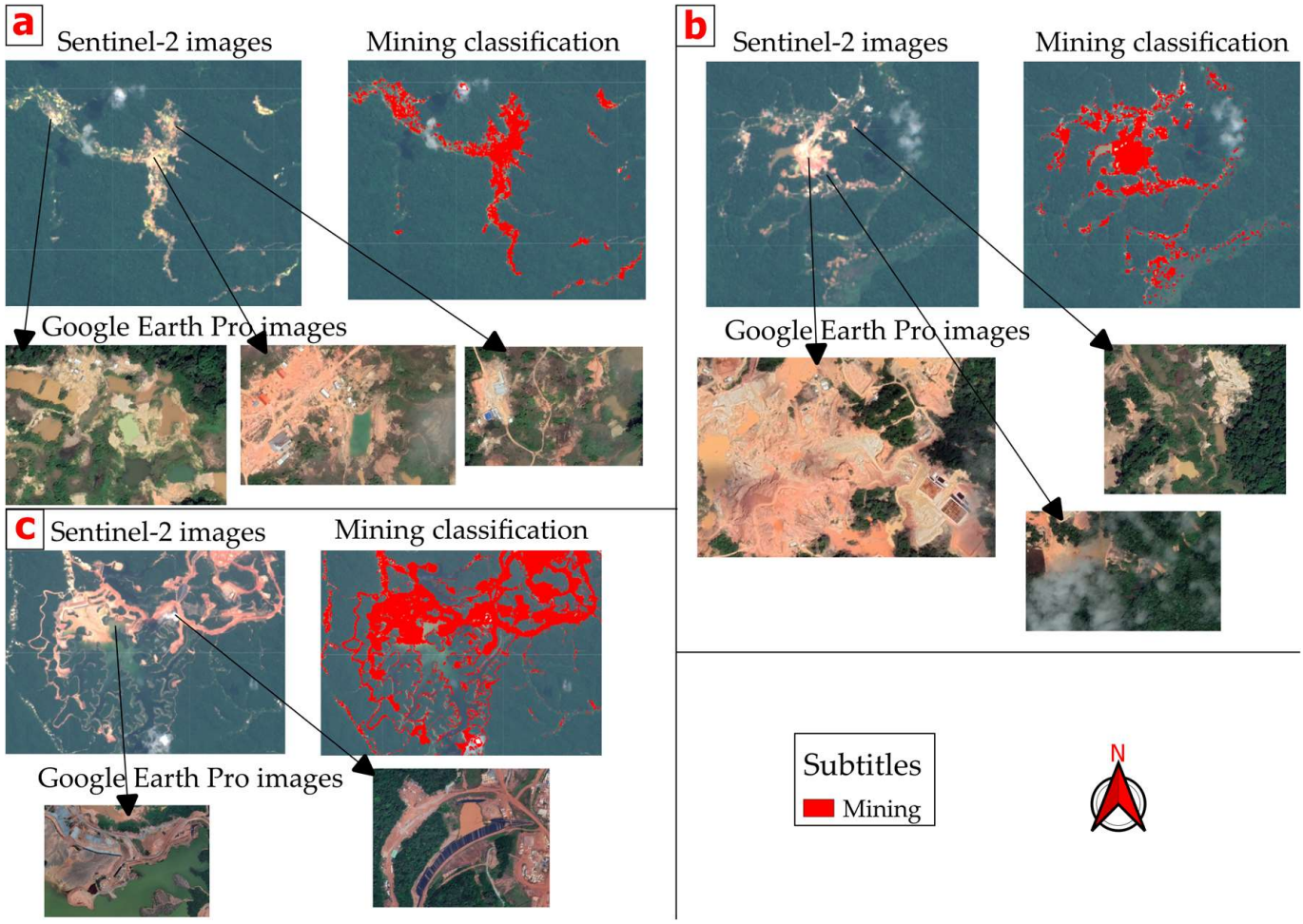

Figure 8. Demonstration of the validation process. From top to bottom: (**a**) first mining point, (**b**) second mining point, and (**c**) third mining point.

Of the 100 validation points established, 80 were correctly classified as mining areas by the CART algorithm, with a kappa index of 0.746, indicating substantial agreement between the classification results and the reference data obtained from high-resolution images using Google Earth Pro.

Table 3 presents a confusion matrix used to evaluate the performance of a classification model. This matrix compares the predictions made by the model with the actual classifica-

tions, based on a dataset containing the 100 validation points. The results are categorized into two classes: "Mining" and "Non-Mining".

Table 3. Confusion matrix table.

	Predicted Mining	**Predicted Non-Mining**	**Total**
Actual Mining	80	5	85
Actual Non-Mining	2	13	15
Total	82	18	100

Of the 82 cases predicted as "Mining", the model got 80 right (true positives) and 2 wrong (false positives). On the other hand, of the 18 cases predicted as "Non-Mining", there were 13 hits (true negatives) and 5 errors (false negatives).

Table 4 presents the performance metrics of the CART model in classifying mining areas, based on 100 validation points. The 97.6% precision indicates the proportion of correct positive predictions, while the 94.1% recall highlights the classification's ability to correctly identify existing mining areas. The F-Score of 95.8% reflects a good balance between precision and recall. Furthermore, the 93% accuracy indicates the proportion of correct predictions in relation to the total number of predictions made by the model.

Table 4. Metrics table.

Metric	**Value**
Precision	97.6%
Recall	94.1%
Accuracy	93%
F-Score	95.8%
Kappa	0.746

The kappa index of 0.746 suggests substantial agreement between the model classifications and the reference data, obtained from high-resolution images from Google Earth Pro. These metrics provide a comprehensive assessment of CART's performance in the specific task of identifying mining areas.

Mapping has proven to be effective in identifying the main components of mining areas (Figure 9) and their associated infrastructure elements, including waste piles; both dams and tailings ponds; airstrips, which are often used for mining and the transport of materials and workers; industrial equipment; mining facilities; and the mineral extraction areas themselves. Furthermore, the classification allowed us to differentiate between active mining areas and the surrounding areas, offering a clear view of the regions of interest and their distinctive characteristics.

After validation, an additional review was carried out of the mining areas identified by the validation samples that were not initially identified by the CART algorithm, as well as the sample areas that were not classified as mining. As a result of this process, 7.25 km^2 of new mining areas was added to the classification, while 1.61 km^2 of previously classified areas was removed. This refined review has significantly contributed to a more accurate representation of areas of mining activity in the region.

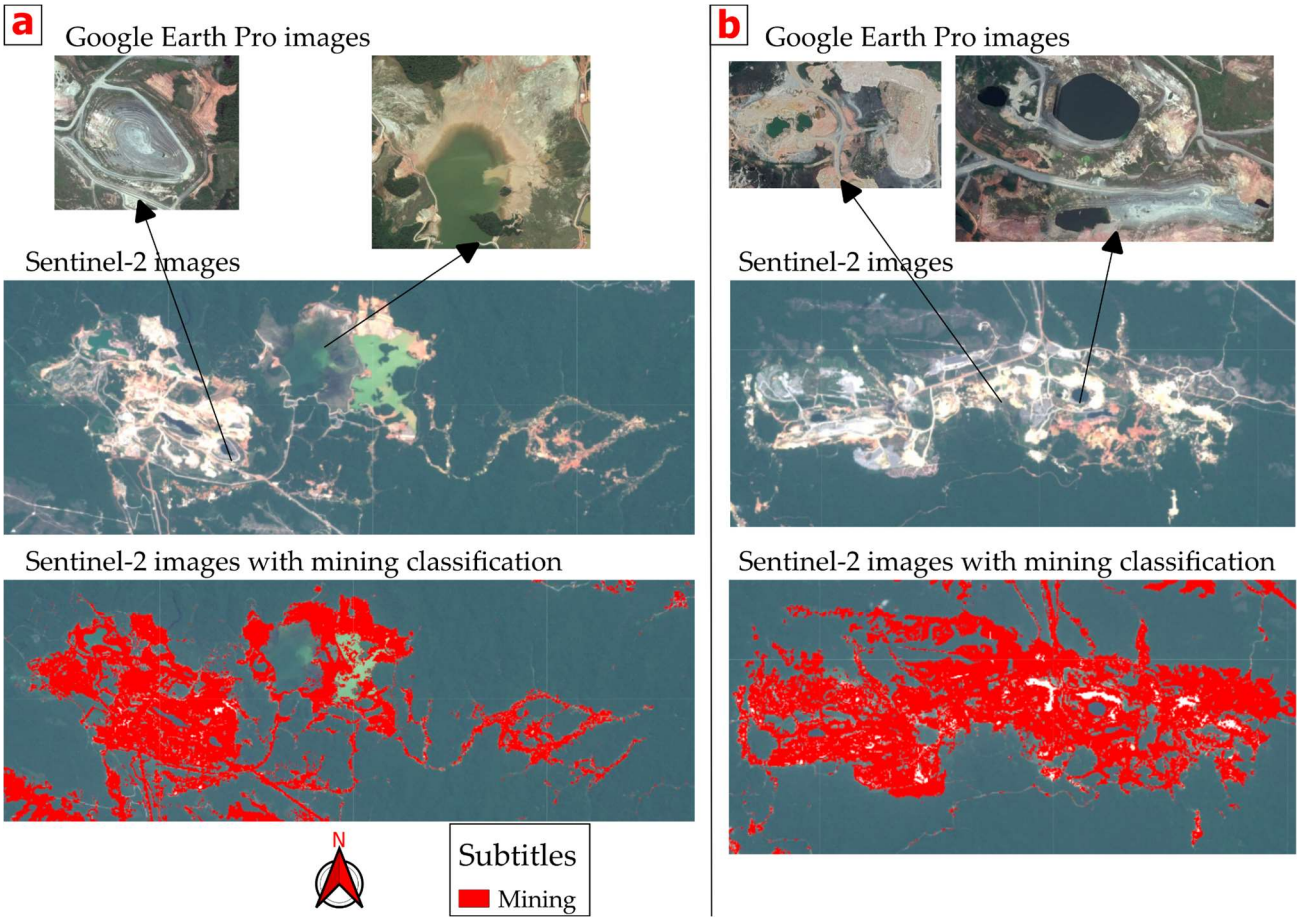

Figure 9. Mapping of mining and associated structures. From left to right: (**a**) first mining point and (**b**) second mining point.

3.2. Total Mining Area

To quantify the extent of areas mapped as mining, each land cover class was analyzed in relation to its total area. Using an area calculation function, it was possible to determine the total mining area over the last 7 years, from 2017 to 2023.

The mapping of these areas was conducted within a polygon covering a total area of 15,882 km^2. This extensive territory was subject to detailed analysis using satellite images acquired over a period of seven years, from 2017 to 2023. Figure 10 below presents the map of mining areas mapped in each year, from 2017 to 2023, highlighting the spatial distribution of mining activities throughout the study period.

The map of mining areas over the years 2017 to 2023 reveals distinct patterns in the distribution and expansion of mining activities. In 2017, mining areas were more concentrated in established mining centers, which served as the focus of activities, with little dispersion in adjacent regions. In 2018, the concentration of activities continued in the main mining centers, although with a slight increase in expansion to nearby areas. This expansion was still limited and did not cover vast areas outside the established centers.

The most notable transition occurred between 2019 and 2020. During this period, mining areas became significantly more sparse. The expansion of mining activities was observed, especially in the lower southeastern arm of Lake Brokopondo, which began to be mined for the first time. This change marked an important dispersion of activities, suggesting an increase in the search for new mining areas outside traditional centers. In 2021, there was a continuation of the dispersion trend observed in 2020, with mining activities spread over a larger area. Although mining centers still remained active, new areas began to be explored.

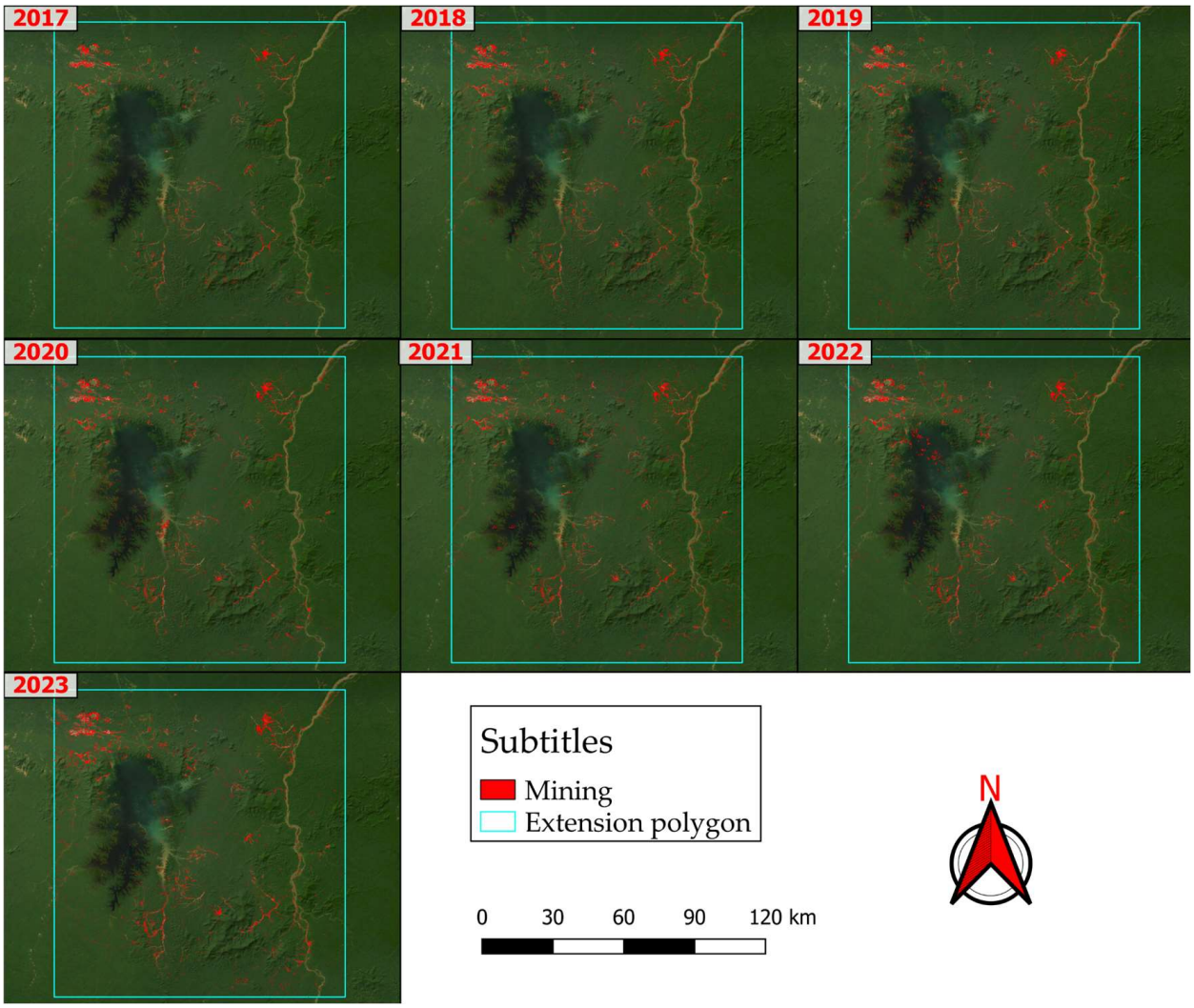

Figure 10. Map of mining mapped in each year, from 2017 to 2023.

From 2022 onwards, there will be a significant increase in mining activities not only in scattered areas, but also in large mining centers. These centers have experienced a renaissance and intensification of operations, reflecting a combination of continuity in existing operations and the addition of new mining activities.

Below, Table 5 describes the total mining area in square kilometers for each year, providing a panoramic view of the expansion or contraction trends in mining activity over the analyzed period.

Table 5. Total area of mining.

Year	2017	2018	2019	2020	2021	2022	2023
Mining (km^2)	148.344724	194.933177	275.098510	231.627975	280.586329	285.746225	296.431852
Mining (m^2)	148344724	194933177	275098510	231627975	280586329	285746225	296431852

Detailed analysis of the data reveals a variation in the total mining area over the years, with increases and decreases in different periods. In 2017, the registered mining area was 148.34 km^2. The following year, there was an increase to 194.93 km^2, indicating an increase of approximately 46.59 km^2. However, in 2019, a more significant increase was observed, reaching 275.10 km^2, which represents a significant increase of 80.17 km^2 compared to the previous year.

In contrast, the year 2020 saw a decrease in the mining area, recording 231.63 km^2, a reduction of approximately 43.47 km^2 compared to 2019. However, this decline was followed by a further increase in 2021, when the mining area reached 280.59 km^2, representing an increase of 48.96 km^2.

In 2022, the total mining area continued to grow, reaching 285.75 km^2. Finally, in 2023, the mining area reached its highest value during the analyzed period, totaling 296.43 km^2.

The following bar graph (Figure 11) presents an overview of the annual variation in the area occupied by mining during the period studied, allowing an understanding of fluctuations in the extent of mining operations over time.

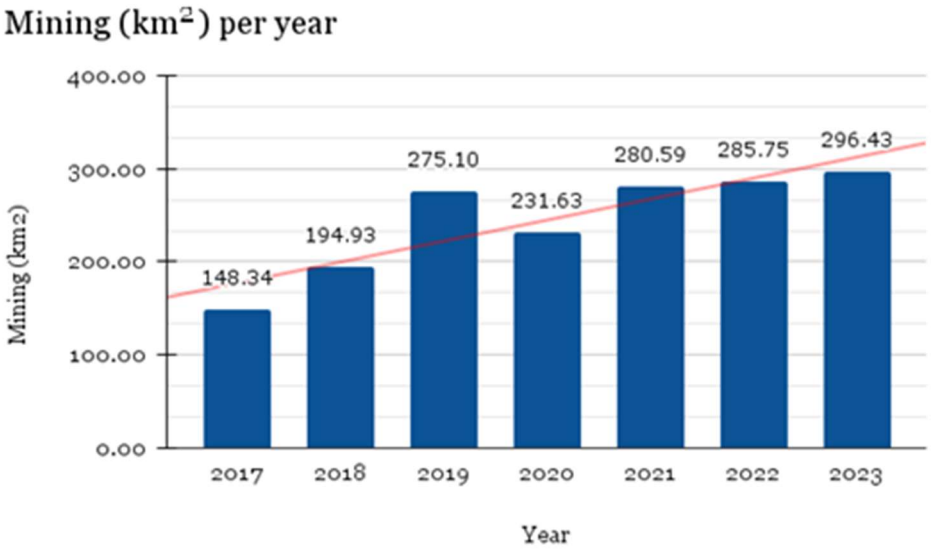

Figure 11. Mining graph by year, from 2017 to 2023.

When comparing the area mined in 2017 with that recorded in 2023, we observed a significant absolute difference of 148.09 km^2, in relation to the average percentage increase in the mined area, and it was found that the average growth rate during this period was approximately 99.23%.

The data reveal that in 2017, mining activity was mainly concentrated in large-scale, industrial mining areas. However, from 2018 onwards, an expansion of alluvial mining areas was observed along the Maroni and Lawa Rivers, as well as in the vicinity of the northeast and southeast arms of Lake Brokopondo, culminating in a significant increase by the year 2019. In 2020, this expansion slowed down, but from 2021 to 2023, there was a resumption of growth, both in areas located more than 500 m from water bodies and in their surroundings.

3.3. Analysis of TSS in Water Bodies in Relation to Mining

The first development of this study consists of the creation of a comprehensive map (Figure 12), highlighting all the water bodies present in the region in question. Additionally, each of these bodies of water was added with an additional layer representing the average TSS during the period from 2017 to 2023. These data were complemented by generating graphs that present points specific to these water bodies, providing a detailed analysis of trends observed over time.

A correlation was observed between the presence of mines in the vicinity of water bodies and the mean TSS and standard deviation values. In regions (Figure 13) where mining activity was detected more, there was a significant increase in average TSS levels, as well as greater variability represented by the standard deviation. These results suggest a direct relationship between mining activity and water quality in these areas.

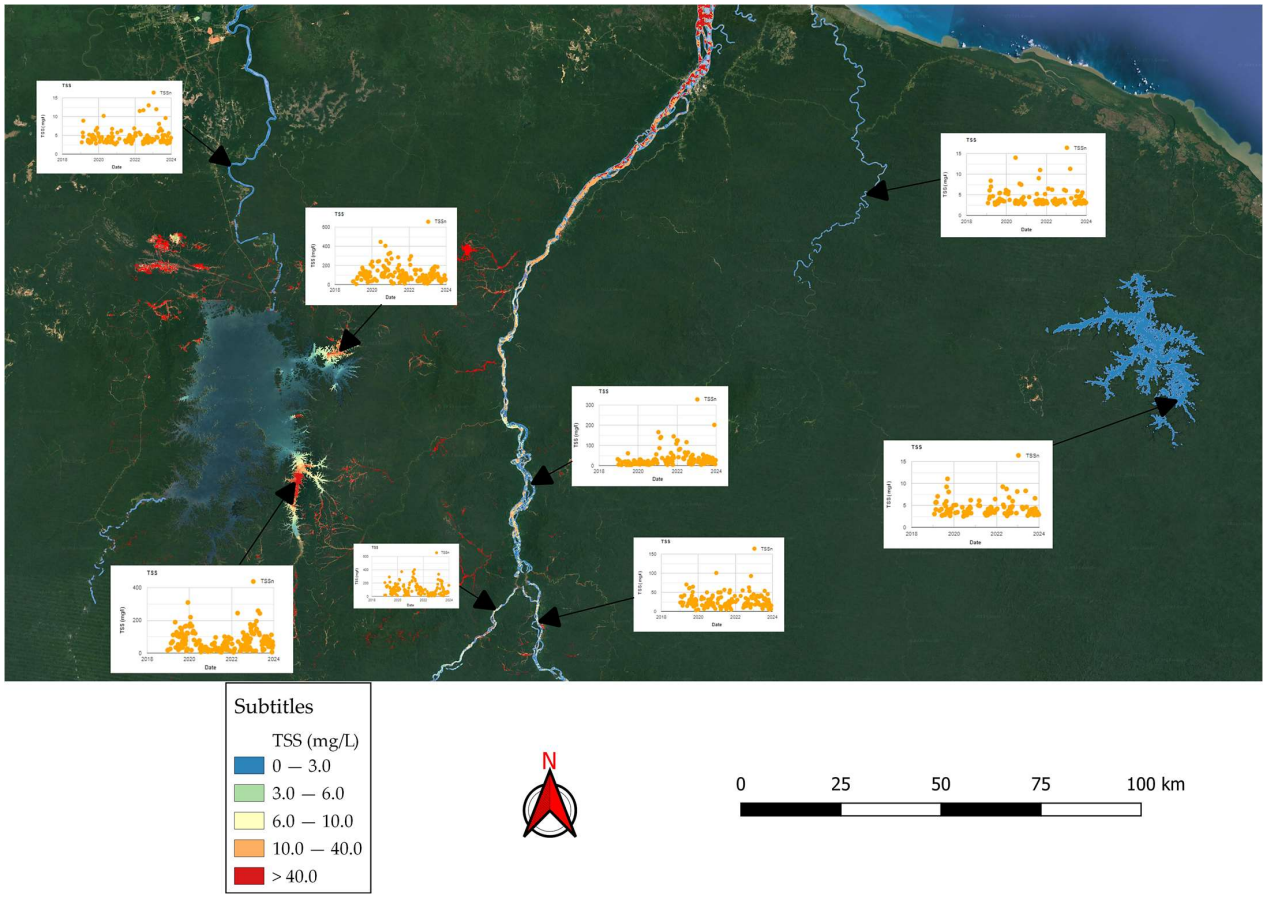

Figure 12. Map with TSS graphs by year (2017 to 2023); water bodies have a band in which each pixel represents its average value over the years studied.

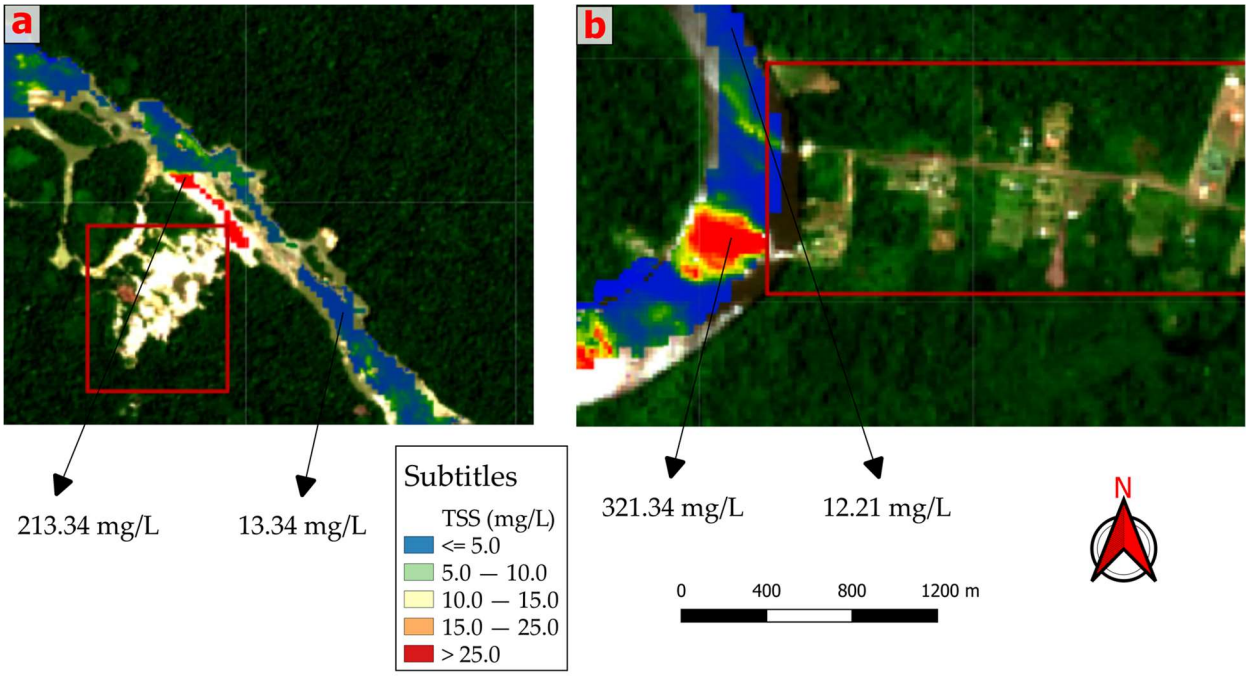

Figure 13. Illustrative figure elucidating mining in two different cases increasing the TSS of the water. From left to right: (**a**) first mining point and (**b**) second mining point.

The standard deviation, in this context, emerges as a crucial metric for understanding the variability in TSS values and their possible origins. It allows us to distinguish whether the observed variations are the result of natural hydrological processes or whether they are associated with siltation caused by mining activity. Notably, water bodies with higher standard deviations were readily related to the presence of mining in their vicinity, highlighting the significant influence of this activity on water quality.

Table 6 presents the average TSS metrics between the years 2017 and 2023 for the water bodies studied.

Table 6. Table of metrics for water bodies.

Water Body	Average TSS (mg/L)	Standard Deviation (mg/L)
Maroni River	45.69	17.75
Suriname River	12.72	8.52
Brokopondo Lake	34.91	21.71
Sinnamary Lake	14.52	5.68

Based on the data presented in this table, we observed significant variations in TSS levels in different bodies of water in the region. The Maroni River stands out with the highest average TSS value, recording 45.69 mg/L, along with the highest standard deviation, indicating considerable variability in TSS levels over time, justified by the CART classification, which displayed several mining polygons along its course, contributing to the load of suspended solids in this body of water.

In the case of Lake Brokopondo, although its average TSS value is slightly lower (34.91 mg/L) than that of the Maroni River, the standard deviation is even higher, indicating an even more significant variability in TSS levels, which is justified by the extensive mining activity in its southeast and northeast branches described previously.

On the other hand, both the Suriname River and Lake Sinnamary exhibit lower average TSS values, recording 12.72 mg/L and 14.52 mg/L, respectively. These two bodies of water in question stand out due to the low number of mining polygons found in their surroundings. In the case of Sinnamary, only 1.81 km^2 of mining was identified in its surroundings, and because this polygon is approximately 3 km from the lake, there was no direct interference with the concentration of solids in this system.

The most critical point of mining activity was identified at Lake Brokopondo (Figure 14). From 2017 to 2023, a gradual increase in the average TSS was observed throughout the period studied. In 2017, the average TSS was recorded at 35 mg/L, and this value increased to 40 mg/L in 2018. The following year, in 2019, there was a further increase, bringing the average TSS to 45 mg/L. In 2020, the increase continued, with the average TSS reaching 50 mg/L. In 2021, the increase appeared to have stabilized, recording an average TSS of 52 mg/L. However, between 2022 and 2023, a significant increase was observed, with the average TSS reaching 60 mg/L in 2023.

Both small-scale artisanal mining activities and larger activities, with industrial instruments, were detected, in which some points where, previously, there were TSS values of 12 mg/L in 2017, now (in 2023), the value was 179 mg/L—a percentage increase of 1391.67%.

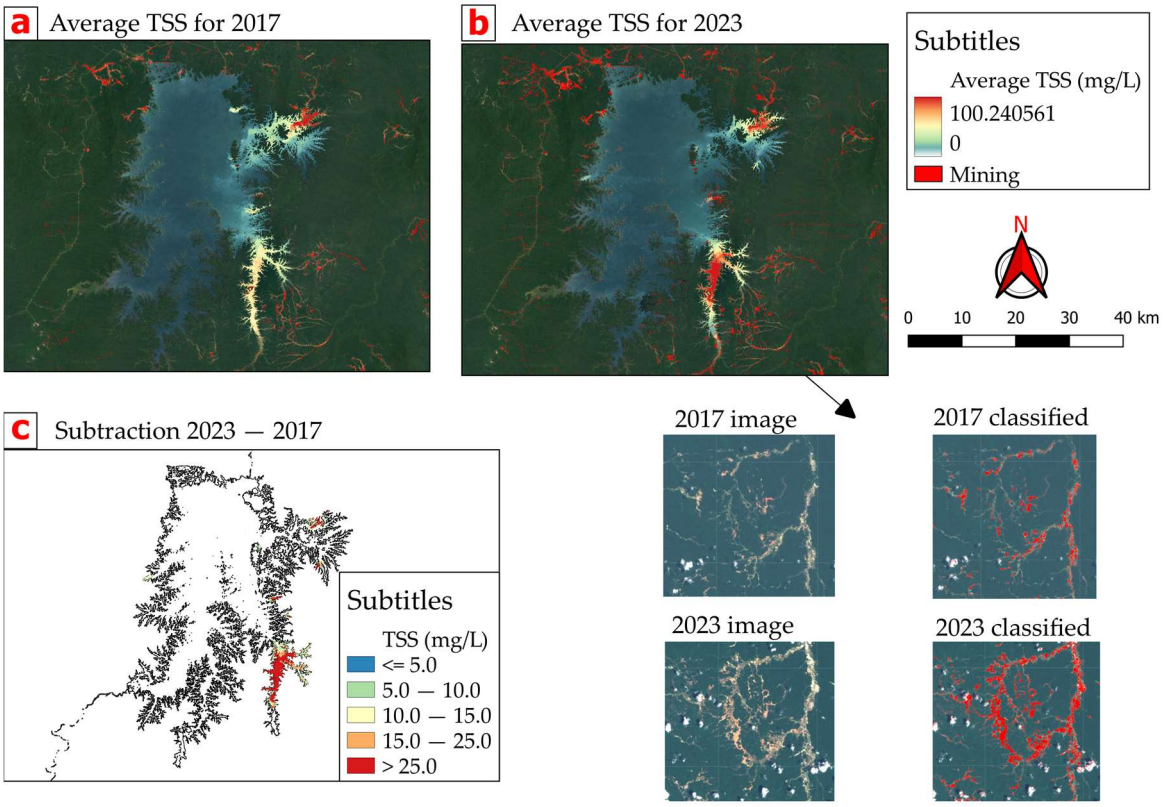

Figure 14. Subtractive map between the years 2023 and 2017. From top left to bottom right: (**a**) TSS average for 2017, (**b**) TSS average for 2023, and (**c**) subtractive image between the two years.

4. Discussion

Using the CART (Classification and Regression Tree) algorithm to map mining areas presents a series of advantages and disadvantages worth discussion.

In terms of advantages, the CART algorithm is known for its ability to handle non-linear data and complex interactions between variables, which is often observed in remote sensing images. Its decision tree-based nature allows an intuitive interpretation of the results, facilitating the understanding of the relationships between the predictor variables and the target class. Furthermore, CART is robust against outliers and can efficiently handle large-scale datasets such as high-resolution satellite images.

On the other hand, the CART classification also has some limitations. One is the tendency to generate complex tree models, which can be difficult to interpret and prone to overfitting, especially when applied to datasets with many explanatory variables. Furthermore, CART's performance can be affected by the inappropriate choice of parameters, such as the maximum number of leaf nodes and maximum tree depth, which can lead to under- or over-fitting models.

In summary, although the CART algorithm is a valuable tool for mining mapping in remote sensing images, it is important to carefully consider its advantages and limitations when interpreting the results and performing subsequent analyses.

Combining the CART algorithm with Sentinel-2A images proved to be an effective strategy, especially considering the low spatial resolution of these images. This low resolution is particularly advantageous for identifying small-scale mining settlements throughout the study area. Sentinel-2A's ability to capture spectral information across multiple bands, coupled with the robust and interpretable nature of the CART algorithm, allows for the more accurate and detailed classification of mining areas, even in locations where activities are smaller in scale. Thus, this union between these two provides a solid approach to mapping and monitoring mining in areas of interest, contributing to a better understanding and management of these environments.

Among the six CART classes used—water, vegetation, deforestation, cloud, cloud shadow, and mining—a notable correlation was observed between the deforestation class and the mining activity in which their differentiation was difficult. This challenge in differentiating between deforestation and mining can be attributed to several reasons, including the spectral similarity between these classes, the overlapping of terrain features, and the complexity of land use changes in the study area, as many deforested areas are converted to mining activities, and vice versa. This difficulty highlights the need for more refined and sensitive approaches for classifying remote sensing images, especially in contexts where the classes of interest have similar spectral characteristics.

When comparing the mining areas along the border between French Guiana and Suriname, a significant distinction is observed. Water bodies located in French Guiana appear to be relatively free from mining activity compared to adjacent areas of Suriname. This difference in the presence of mining is reflected in the water quality of water bodies, especially in relation to the TSS. Areas less affected by mining have lower TSS levels, indicating potentially better water quality compared to areas most impacted by mining activity.

The most critical point of mining activity was identified at Lake Brokopondo. The presence of mining operations in its proximity raises concerns about possible water pollution, habitat destruction, and changes in water quality, which could have far-reaching consequences for both aquatic life and neighboring communities. Therefore, effective environmental management strategies are essential to mitigate the adverse effects of mining activities on Lake Brokopondo and preserve its ecological integrity.

The abundant availability of Google Earth Engine (GEE) imagery provides a significant advantage for detailed spatiotemporal analyses across diverse study areas. The ability to access a wide range of satellite images quickly and efficiently allows analysis to be carried out over time with unprecedented spatial and temporal resolution. This wealth of data was critical to our research, enabling a comprehensive investigation of mining patterns and their impacts on water bodies over a seven-year period. The codes created in GEE for this article were provided in the Supplementary Materials.

Finally, the continued relevance of using remote sensing technologies, such as GEE, and innovative methodological approaches to monitor and manage natural resources in a sustainable way is highlighted. These tools and techniques are essential to guide environmental management policies and practices that aim to conserve and protect vulnerable aquatic ecosystems from human activities, such as mining.

Supplementary Materials: The codes used are available at the following links: 3.2. Total Mining Area—https://code.earthengine.google.com/f00df439945c56e560e8cfb75475c54a (accessed on 10 July 2024). 3.3. Analysis of TSS in Water Bodies in Relation to Mining—https://code.earthengine.google.com/363ec3be617e1c0a8ee61a318164fda1 (accessed on 10 July 2024).

Author Contributions: Conceptualization, B.M.P.; methodology, B.M.P. and F.d.L.L.; validation, B.M.P.; formal analysis, B.M.P.; investigation, B.M.P. and F.d.L.L.; resources, B.M.P. and F.d.L.L.; writing—original draft preparation, B.M.P. and F.d.L.L.; writing—review and editing, B.M.P. and F.d.L.L.; visualization, B.M.P. and F.d.L.L.; supervision, B.M.P. and F.d.L.L.; funding acquisition, B.M.P. and F.d.L.L. All authors have read and agreed to the published version of the manuscript.

Funding: This research received no external funding.

Data Availability Statement: The original contributions presented in the study are included in the article, and further inquiries can be directed to the corresponding author.

Conflicts of Interest: The authors declare no conflicts of interest.

References

1. Rozo, S.V. Unintended effects of illegal economic activities: Illegal gold mining and malaria. *World Dev.* **2020**, *136*, 105119. [CrossRef]
2. Veiga, M.M.; Maxson, P.A.; Hylander, L.D. Origin and consumption of mercury in small-scale gold mining. *J. Clean. Prod.* **2006**, *14*, 436–447. [CrossRef]
3. Veiga, M.M. *Mercury in Artisanal Gold Mining in Latin America: Facts, Fantasies and Solutions*; UNIDO: Vienna, Austria, 1997.

4. Sousa, R.N.; Veiga, M.M. Using performance indicators to evaluate an environmental education program in artisanal gold mining communities in the Brazilian amazon. *Ambio* **2009**, *38*, 40–46. [CrossRef] [PubMed]
5. Telmer, K.; Stapper, D. *Evaluating and Monitoring Small Scale Gold Mining and Mercury Use: Building a Knowledge-Base with Satellite Imagery and Field Work*; United Nations Industrial Development Organization: Victoria, BC, Canada, 2007.
6. Fernandes, F.R.C.; Alamino, R.D.C.J.; Araújo, E.R. *Recursos Minerais E Comunidade: Impactos Humanos, Socioambientais E Econômicos*; CETEM/MCTI: Rio de Janeiro, Brazil, 2014.
7. World Wildlife Fund. Extracted Forests—Unearthing the Role of Mining-Related Deforestation as a Driver of Global. Available online: https://policycommons.net/artifacts/3533626/extracted-forests/4334839/fragments/ (accessed on 27 June 2024).
8. World Bank. *2023 State of the Artisanal and SmallScale Mining Sector*; World Bank: Washington, DC, USA, 2023.
9. Rodrigues, R.M.; Mascarenhas, A.F.S.; Ichihara, A.H.; Souza, T.M.C. *Estudo Dos Impactos Ambientais Decorrentes do Extrativismo Mineral E Poluição Mercurial no TAPAJÓS—Pré-Diagnóstico*; CETEM/CNPq: Rio de Janeiro, Brazil, 1994.
10. Roland, F.; Esteves, F.D. Effects of bauxite tailing on PAR attenuation in an amazonian crystalline water lake. *Hydrobiologia* **1998**, *377*, 1–7. [CrossRef]
11. Mol, J.H.; Ouboter, P.E. Downstream effects of erosion from small-scale gold mining on the instream habitat and fish community of a small neotropical rainforest stream. *Conserv. Biol.* **2004**, *18*, 201–214. [CrossRef]
12. Tudesque, L.; Grenouillet, G.; Gevrey, M.; Khazraie, K.; Brosse, S. Influence of small-scale gold mining on french guiana streams: Are diatom assemblages valid disturbance sensors? *Ecol. Indic.* **2012**, *14*, 100–106. [CrossRef]
13. Grimaldi, M.; Guédron, S.; Grimaldi, C. Impact of gold mining on mercury contamination and soil degradation in Amazonian ecosystems of French Guiana. In *Land-Use Change Impacts on Soil Processes: Tropical and Savannah Ecosystems*; CABI: Wallingford, UK, 2015.
14. Shanks, G.D.; Wongsrichanalai, C. Mining-associated malaria epidemics. *Am. J. Trop. Med. Hyg.* **2022**, *106*, 33. [CrossRef] [PubMed]
15. Earth Engine Data Catalog. Harmonized Sentinel-2 MSI: MultiSpectral Instrument, Level-2A. Available online: https://developers.google.com/earth-engine/datasets/catalog/COPERNICUS_S2_SR_HARMONIZED#bands (accessed on 27 June 2024).
16. Binding, C.E.; Bowers, D.G.; Mitchelson-Jacob, E.G. Estimating suspended sediment concentrations from ocean colour measurements in moderately turbid waters; the impact of variable particle scattering properties. *Remote Sens. Environ.* **2005**, *94*, 373–383. [CrossRef]
17. Harrington, J.A.; Schiebe, F.R.; Nix, J.F. Remote sensing of Lake Chicot, Arkansas: Monitoring suspended sediments, turbidity, and Secchi depth with Landsat MSS data. *Remote Sens. Environ.* **1992**, *39*, 15–27. [CrossRef]
18. Lobo, F.L.; Costa, M.P.; Novo, E.M. Time-series analysis of Landsat-MSS/TM/OLI images over Amazonian waters impacted by gold mining activities. *Remote Sens. Environ.* **2015**, *157*, 170–184. [CrossRef]
19. Albert, A.; Mobley, C.D. An analytical model for subsurface irradiance and remote sensing reflectance in deep and shallow case-2 waters. *Opt. Express* **2003**, *11*, 2873–2890. [CrossRef] [PubMed]
20. Doxaran, D.; Ehn, J.; Bélanger, S.; Matsuoka, A.; Hooker, S.; Babin, M. Optical characterisation of suspended particles in the Mackenzie River plume (Canadian Arctic Ocean) and implications for ocean colour remote sensing. *Biogeosciences* **2012**, *9*, 3213–3229. [CrossRef]
21. Mertes LA, K.; Smith, M.O.; Adams, J.B. Estimating suspended sediment concentrations in surface waters of the Amazon River wetlands from landsat images. *Remote Sens. Environ.* **1993**, *43*, 281–301. [CrossRef]